

NANO EXPRESS

Open Access



Sulfate Exchange of the Nitrate-Type Layered Hydroxide Nanosheets of $\text{Ln}_2(\text{OH})_5\text{NO}_3 \cdot n\text{H}_2\text{O}$ for Better Dispersed and Multi-color Luminescent Ln_2O_3 Nanophosphors (Ln = $\text{Y}_{0.98}\text{RE}_{0.02}$, RE = Pr, Sm, Eu, Tb, Dy, Ho, Er, and Tm)

Xiaoli Wu^{1,3}, Weigang Liu¹, Ji-Guang Li^{1,2*}, Qi Zhu¹, Xiaodong Li¹ and Xudong Sun¹

Abstract

Through restricting thickness growth by performing coprecipitation at the freezing temperature of $\sim 4^\circ\text{C}$, solid-solution nanosheets (up to 5-nm thick) of the $\text{Ln}_2(\text{OH})_5\text{NO}_3 \cdot n\text{H}_2\text{O}$ layered hydroxide (Ln = $\text{Y}_{0.98}\text{RE}_{0.02}$; RE = Pr, Sm, Eu, Tb, Dy, Ho, Er, and Tm, respectively) were directly synthesized without performing conventional exfoliation. In situ exchange of the interlayer NO_3^- with SO_4^{2-} produced a sulfate derivative [$\text{Ln}_2(\text{OH})_5(\text{SO}_4)_{0.5} \cdot n\text{H}_2\text{O}$] of the same layered structure and two-dimensional crystallite morphology but substantially contracted d_{002} basal spacing (from ~ 0.886 to 0.841 nm). The sulfate derivative was systematically compared against its nitrate parent in terms of crystal structure and phase/morphology evolution upon heating. It is shown that the interlayer SO_4^{2-} , owing to its bonding with the hydroxide main layer, significantly raises the decomposition temperature from ~ 600 to 1000°C to yield remarkably better dispersed oxide nanopowders via a monoclinic $\text{Ln}_2\text{O}_2\text{SO}_4$ intermediate. The resultant $(\text{Y}_{0.98}\text{RE}_{0.02})_2\text{O}_3$ nanophosphors were studied for their photoluminescence to show that the emission color, depending on RE^{3+} , spans a wide range in the Commission Internationale de l'Éclairage (CIE) chromaticity diagram, from blue to deep red via green, yellow, orange, and orange red.

Keywords: Nanosheets, Anion exchange, Phase evolution, Oxide phosphor, Luminescence

Background

Y_2O_3 is a widely used host lattice in the phosphor field, owing to its excellent structure stability, chemical durability, and particularly its ability to accept a substantial amount of various trivalent rare-earth activators for a broad range of optical functionalities. Due to their technical importance in the lighting and display areas, Y_2O_3 -based phosphors are being widely investigated to

correlate their luminescent performance with the characteristics of the phosphor powder [1, 2]. Controllable synthesis has always been an active area of phosphor study, and the well-adopted processing technologies may include flux-assisted solid state reaction [3, 4], solution synthesis, combustion [5], spray pyrolysis [6–8], and gas-phase condensation [9, 10].

Among the aforementioned synthetic strategies, solution processing is of particular interest since it allows a facile manipulation of particle morphology. With this technique, Y_2O_3 -based phosphors that have the various morphologies of zero-dimensional (0D) nanoparticles, monodispersed microspheres [11, 12], 1D nanowires/nanotubes [13–15], 2D nanoplates [16–18], and hierarchical structures [2, 19] have been obtained. As the

* Correspondence: LJiguang@nims.go.jp

¹Key Laboratory for Anisotropy and Texture of Materials (Ministry of Education), School of Materials Science and Engineering, Northeastern University, Shenyang, Liaoning 110819, China

²Materials Processing Unit, National Institute for Materials Science, Tsukuba, Ibaraki 305-0044, Japan

Full list of author information is available at the end of the article

direct product of solution synthesis is usually a precursor, the final phosphor oxide is thus frequently observed to have properties dependent on the characteristics of its precursor [2]. Layered rare-earth hydroxide (LRH), as a relatively new type of anionic layered compounds [20], has attracted much attention during the recent years owing to its unique combination of the layered structure and the abundant optical, magnetic, and catalytic properties of the rare-earth elements [21–34]. The crystal structure of $\text{Ln}_2(\text{OH})_5\text{A}\cdot n\text{H}_2\text{O}$ LRH (Ln = rare-earth; $\text{A} = \text{NO}_3^-$ or halogen anion; $n \sim 1.5$) can be viewed as an alternative stacking along the c -axis ([001] direction) of the positively charged hydroxide main layers containing Ln^{3+} and exchangeable A anions located in the interlayer for charge balance. The well-established synthetic methodologies of hydrothermal reaction [25–34] and reflux growth [21–24] generally produce platelike LRH crystals of several microns in lateral dimension and tens to hundreds of nanometers in thickness, for which single layer or few-layer thick nanosheets can only be obtained by swelling the pristine crystals via exchange of the interlayer anions with significantly larger ones (such as dodecyl sulfate, DS^-), followed by exfoliation in a proper medium (such as formamide) under mechanical agitation [35–39]. Exfoliation, however, is well known to be time consuming, frequently incomplete, and usually accompanied by fragmentation of nanosheets. We previously reported a capped growth technique to synthesize nanometer-thin LRH flakes via one-step hydrothermal reaction [32], but the batch yield is rather limited. Both the pristine LRH crystals and the exfoliated nanosheets can serve as new precursors for oxide phosphors and phosphor films [35–39], but thick crystallites would not collapse into nanoparticles via calcination and the resultant oxides frequently retain platelike morphologies [40–42].

The hydroxide main layer of LRH is a close-packed low-energy plane, and thus, its two-dimensional growth needs lower activation energy than the thickness growth along the [001] direction. We recently demonstrated that, through suppressing thickness growth by lowering the synthesis temperature to $\sim 4^\circ\text{C}$, NO_3^- -LRH nanosheets of only ~ 4 -nm thick can be directly crystallized, without exfoliation, for a wide spectrum of single Ln ($\text{Ln} = \text{Pr}$ - Er , and Y) [43]. With this technique, similarly thin nanosheets were produced in this work for the LRH solid solutions of Y/RE ($\text{RE} = \text{Pr}$, Sm , Eu , Tb , Dy , Ho , Er , and Tm) in good batch quantity (0.03 mol of LRH or ~ 10 g). The effects of SO_4^{2-} exchange for interlayer NO_3^- on crystal structure and thermal behavior of the nanosheets and also characteristics and luminescent properties of the derived $(\text{Y}_{0.98}\text{RE}_{0.02})_2\text{O}_3$ nanophosphors were studied in detail.

Methods

Freezing Temperature Crystallization of LRH Solid-Solution Nanosheets

The starting rare-earth sources are Pr_6O_{11} (99.96 % pure), Tb_4O_7 (99.99 % pure), and RE_2O_3 (99.99 % pure, $\text{RE} = \text{Y}$, Sm , Eu , Dy , Ho , Er , and Tm), all were purchased from Huizhou Ruier Rare-Chem. Hi-Tech. Co. Ltd (Huizhou, China). The other reagents of ammonium hydroxide solution (25 %), nitric acid (63 wt.%), and ammonium sulfate are of analytical grade and were purchased from Shenyang Chemical Reagent Factory (Shenyang, China). Nitrate solution of the rare earth was prepared by dissolving the oxide with a proper amount of nitric acid, followed by evaporation to dryness at 95°C to remove superfluous HNO_3 and a final dilution to 1.0 mol/L.

In a typical synthesis, a diluted ammonium hydroxide solution (1.0 mol/L) was slowly dripped (~ 2.0 mL/min) into 300 mL of a 0.2 mol/L nitrate solution of Ln^{3+} ($\text{Ln} = \text{Y}_{0.98}\text{RE}_{0.02}$) kept at $\sim 4^\circ\text{C}$ until pH ~ 8 to produce $\text{Ln}_2(\text{OH})_5\text{NO}_3\cdot n\text{H}_2\text{O}$ nanosheets (30 mmol of $\text{Ln}_2(\text{OH})_5\text{NO}_3\cdot n\text{H}_2\text{O}$ per batch) [43]. For anion exchange with SO_4^{2-} –100 mL aqueous solution containing 15 mmol of $(\text{NH}_4)_2\text{SO}_4$ (one SO_4^{2-} would replace two NO_3^-) was added into the nanosheets suspension after 20 min of magnetic stirring (in situ anion exchange). The final product was collected via centrifugation after reaction for 1 h, followed by sequential washing with distilled water three times and ethanol one time and then air drying at 50°C for 15 h. Calcination of the dried nanosheets was performed in flowing oxygen gas (200 mL/min), using a heating rate of $5^\circ\text{C}/\text{min}$ at the ramp stage and a holding time of 4 h. The final phosphor powders are all calcined at 1100°C , but with the Pr- and Tb-containing samples being subjected to an additional reduction in flowing H_2 (200 mL/min) at 1100°C for 1 h.

Characterization Techniques

Chemical analysis of the products was performed for Ln via inductively coupled plasma (ICP) spectroscopy (Model IRIS Advantage, Jarrell-Ash Japan, Kyoto), for NO_3^- via spectrophotometry (Ubest-35, Japan Spectroscopic Co., Ltd., Tokyo), and for S via combustion-infrared absorptiometry (Model CS-444LS, LECO, St. Joseph, MI). The detection limits of these analyses are all 0.01 wt.%. Phase identification was made via X-ray diffractometry (XRD; Model PW3040/60, Panalytical B.V., Almelo, the Netherlands) operated at 40 kV/40 mA, using nickel-filtered $\text{Cu-K}\alpha$ radiation ($\lambda = 0.15406$ nm) and a scanning speed of $1.0^\circ 2\theta/\text{min}$. Fourier transform infrared spectroscopy (FTIR; Model Spectrum RXI, Perkin-Elmer, Shelton, CT) was performed by the standard KBr method. Powder morphology was analyzed by transmission electron microscopy under an

acceleration voltage of 200 kV (TEM; Model JEM-2000FX, JEOL, Tokyo) and field emission scanning electron microscopy (FE-SEM; Model S-5000, Hitachi, Tokyo) under 10 kV. Thermogravimetry (TG; Model 8120, Rigaku, Tokyo) of the nanosheets was conducted in flowing air (100 mL/min) with a constant heating rate of 10 °C/min. Specific surface area of the oxide phosphor was obtained with an automatic analyzer (Model TriStar II 3020, Micromeritics Instrument Corp., Norcross, GA) using the Brunauer-Emmett-Teller (BET) method via nitrogen adsorption at 77 K. Particle size/size distribution analysis was made with a laser-diffraction particle sizer (Model LA-920, Horiba Scientific, Kyoto), after ultrasonically dispersing the oxide powder in ethanol. Photoluminescence was analyzed at room temperature using an FP-6500 fluorospectrophotometer (JASCO, Tokyo) equipped with a

60-mm-diameter integrating sphere (Model ISF-513, JASCO) and a 150-W Xe-lamp for excitation. Measurements were conducted under identical conditions for all the samples, using a scan speed of 100 nm/min and slit widths of 5 nm for both excitation and emission. Fluorescence lifetime of the luminescence was analyzed with the FP-6500 equipment for Sm^{3+} , Eu^{3+} , and Tb^{3+} , and with a DeltaFlex lifetime fluorescence spectrometer (Horiba Scientific) for the fast decay of Pr^{3+} , Dy^{3+} , Ho^{3+} , Er^{3+} , and Tm^{3+} .

Results and Discussion

Characteristics of the NO_3^- -LLnH Nanosheets and the Effects of SO_4^{2-} Exchange

The effects of SO_4^{2-} exchange on the crystal structure of LLnHs were analyzed with $\text{L}(\text{Y}_{0.98}\text{Eu}_{0.02})\text{H}$ for example. Figure 1a compares XRD patterns of the NO_3^- -

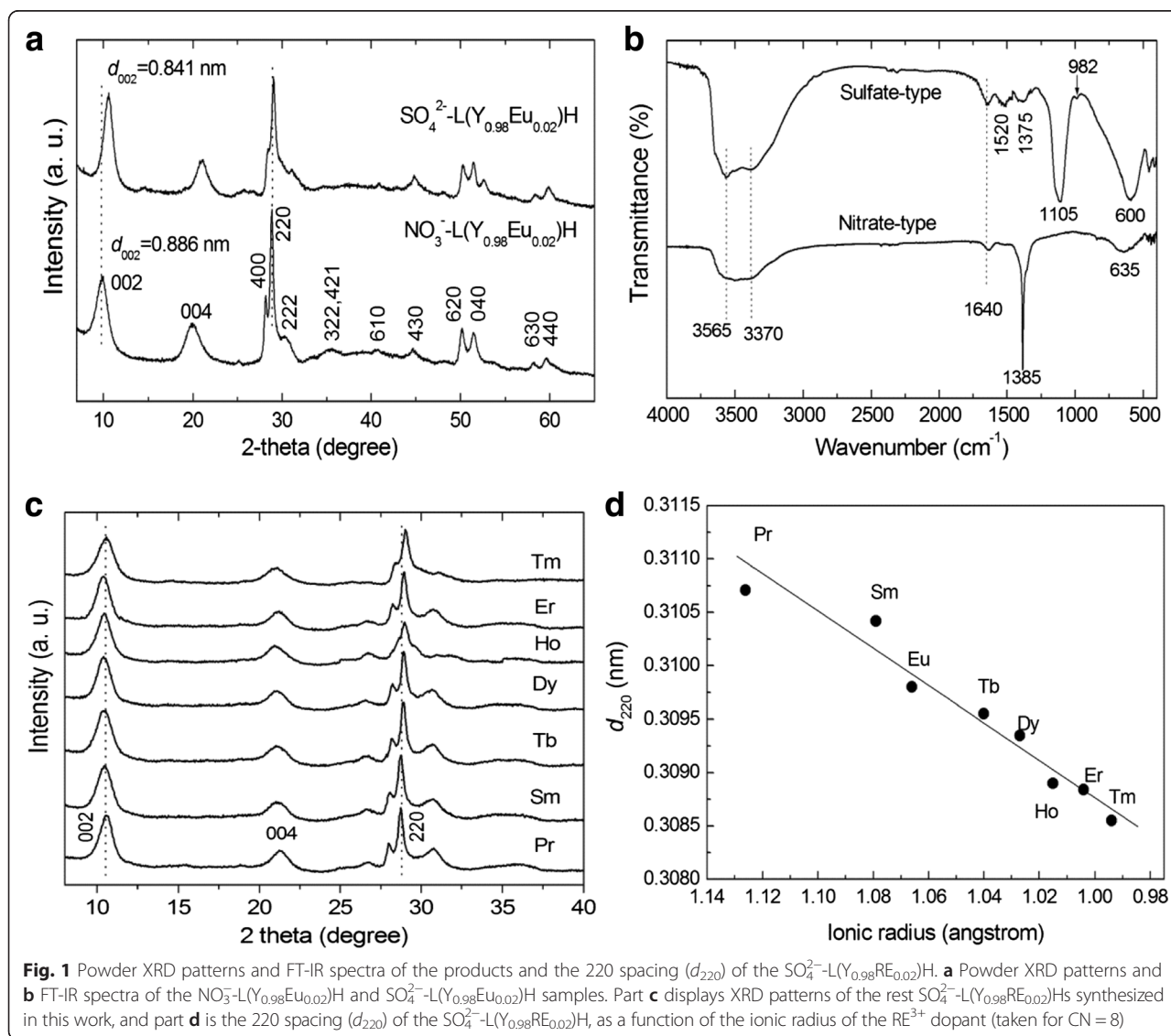


Fig. 1 Powder XRD patterns and FT-IR spectra of the products and the 220 spacing (d_{220}) of the $\text{SO}_4^{2-}\text{-L}(\text{Y}_{0.98}\text{RE}_{0.02})\text{H}$. **a** Powder XRD patterns and **b** FT-IR spectra of the $\text{NO}_3^-\text{-L}(\text{Y}_{0.98}\text{Eu}_{0.02})\text{H}$ and $\text{SO}_4^{2-}\text{-L}(\text{Y}_{0.98}\text{Eu}_{0.02})\text{H}$ samples. Part **c** displays XRD patterns of the rest $\text{SO}_4^{2-}\text{-L}(\text{Y}_{0.98}\text{RE}_{0.02})\text{H}$ s synthesized in this work, and part **d** is the 220 spacing (d_{220}) of the $\text{SO}_4^{2-}\text{-L}(\text{Y}_{0.98}\text{RE}_{0.02})\text{H}$, as a function of the ionic radius of the RE^{3+} dopant (taken for CN = 8)

$L(Y_{0.98}Eu_{0.02})H$ and its SO_4^{2-} derivative. The NO_3^- -type exhibits the characteristic $00l$ and non- $00l$ diffractions of $Ln_2(OH)_5NO_3 \cdot nH_2O$ layered compounds [20–34]. The strong and sharp 220 diffraction, arising from the ab plane (the hydroxide main layer), suggests that the host layers of $L(Y_{0.98}Eu_{0.02})H$ are well crystallized. Compared with the thick LRH crystals synthesized under high temperature [21–31, 33, 34], the 002 diffraction has a substantially lower intensity relative to the 220 one, implying that the primary crystallites are much less developed along the c -axis or rather thin, as also confirmed later by TEM analysis. SO_4^{2-} exchange of NO_3^- shortens the interlayer distance, as perceived from the obvious shifting of the $00l$ diffraction to a higher angle, and the basal spacing (d_{002}) calculated from the center of the 002 peak is ~ 0.886 nm for $NO_3^-L(Y_{0.98}Eu_{0.02})H$ and 0.841 nm for the SO_4^{2-} derivative. The values are close to those found for NO_3^-LYH and its exchange product, respectively [43]. The sulfate derivative still exhibits quite strong 220 diffraction, indicating that sulfate exchange did not appreciably damage the hydroxide main layers. Shifting of the 220 peak from $2\theta \sim 28.86^\circ$ to 29.02° and decreased intensity of the 400 diffraction by the anion exchange, however, suggests that the intercalated SO_4^{2-} is interacting with the hydroxide layers to deteriorate crystallinity of the sample. The interaction, mostly through hydrogen bonding with the hydroxyls/ H_2O in the $[Ln(OH)_7H_2O]$ and $[Ln(OH)_8H_2O]$ polyhedrons that comprise the hydroxide layers [21–24], leads to lattice distortion and thus the slight peak-shifting [43]. The hydrogen bonding is also responsible for the observed interlayer contraction, since it would draw closer the adjacent positively charged hydroxide layers [43].

Chemical analysis of the $NO_3^-L(Y_{0.98}Eu_{0.02})H$ found ~ 1.65 wt.% of Eu, 49.88 wt.% of Y, and 16.68 wt.% of NO_3^- , corresponding to Y/Eu and NO_3^-/Ln ($Ln = Y$ and Eu) molar ratios of 0.98/0.019 and 0.94/2 (close to 1/2), respectively. The results thus confirm that the prescribed Y/Eu atomic ratio (0.98/0.02) has essentially been kept to the product and $NO_3^-L(Y_{0.98}Eu_{0.02})H$ has been formed. The SO_4^{2-} exchange product was found to have ~ 1.87 wt.% of Eu, 51.17 wt.% of Y, 4.50 wt.% of S, and trace NO_3^- (0.18 wt.%), which lead to Y/Eu and SO_4^{2-}/Ln molar ratios of 0.98/0.021 and 0.48/2 (close to 0.5/2), respectively. The outcomes thus indicate that the anion exchange did not appreciably alter the Y/Eu ratio, and SO_4^{2-} exchange of the interlayer NO_3^- is virtually complete. The results of the chemical analysis conform to those of FTIR spectroscopy (Fig. 1b). It is clearly seen that the intense NO_3^- absorption at ~ 1385 cm^{-1} (ν_3 vibration, as of free anion) vanished, and meanwhile the ν_3 (~ 1105 cm^{-1}) and ν_1 (~ 982 cm^{-1}) absorptions, being characteristic of SO_4^{2-} , appeared from the exchange product. The non-splitting

feature of ν_3 suggests that SO_4^{2-} is not directly coordinated to the metal center in the hydroxide layer while the emergence of ν_1 implies that the SO_4^{2-} tetrahedron is distorted owing to the effects of hydrogen bonding [43–45]. It is also owing to the effects of hydrogen bonding that the stretching vibrations of hydroxyls (~ 3565 cm^{-1}) and the O–H radicals in hydration water (~ 3370 cm^{-1}) are both substantially enhanced [44, 45]. The twin absorption bands at ~ 1520 and 1375 cm^{-1} indicate contamination of the product by CO_3^{2-} , mostly from dissolved atmospheric CO_2 during synthesis. All the SO_4^{2-} -LLnHs made in this work show almost identical interlayer distances owing to the limited content of RE, but the 220 diffraction successively shifts towards a higher angle along with the decreasing ionic size of the RE^{3+} dopant (Fig. 2c). The 220 spacing (d_{220}) is shown in Fig. 2d as a function of RE^{3+} size (for eightfold coordination) [46]. As the 220 diffraction reflects metal-to-metal distance in the hydroxide layer [21–24], the d_{220} value thus monotonically decreases towards a smaller RE^{3+} as expected. The results also provide direct evidence of solid-solution formation.

Figure 2 shows the results of electron microscopy for the two types of $L(Y_{0.98}Eu_{0.02})Hs$. FE-SEM observation found that the $NO_3^-L(Y_{0.98}Eu_{0.02})H$ is composed of 3D flower-like assemblies of nanoflakes having lateral dimensions up to ~ 300 nm (Fig. 2a, coated with 10-nm-thick tungsten for electrical conduction), while TEM analysis found entangled nanosheets of up to ~ 5 -nm thick (the inset). Calculated from the d_{002} basal spacing of ~ 0.886 nm, each single nanosheet would have only ~ 5 – 6 stacking repetitions along the c -axis. Selected area electron diffraction (SAED) yielded a well-arranged spot-like pattern (the inset) for the hydroxide layer, indicating that the individual nanosheets are primary of single crystalline and are well crystallized. Anion exchange with SO_4^{2-} did not incur any appreciable morphology change to either the overall flower-like assemblies or the individual nanosheets (Fig. 2b), in compliance with our previous observations on NO_3^-LYH [43].

Decomposition and Phase/Morphology Evolution of the Nanosheets upon Heating

Thermal behaviors of the nanosheets were analyzed via TG, and the results are compared in Fig. 3 for the $NO_3^-L(Y_{0.98}Eu_{0.02})H$ and $SO_4^{2-}L(Y_{0.98}Eu_{0.02})H$. The NO_3^- type clearly decomposes via three well-defined stages as previously observed for thick LRH crystals [25–29, 32–34], with the first one being dehydration to form $Ln_2(OH)_5NO_3$ (up to ~ 175 $^\circ C$), the second one being dehydroxylation to yield an intermediate mass with nominal composition of $(Y_{0.98}Eu_{0.02})_2O_2(OH)NO_3$ (up to ~ 325 $^\circ C$), and the last one being further dehydroxylation and denitration to form oxide (up to ~ 545 $^\circ C$). Though the NO_3^-LLnH obtained in

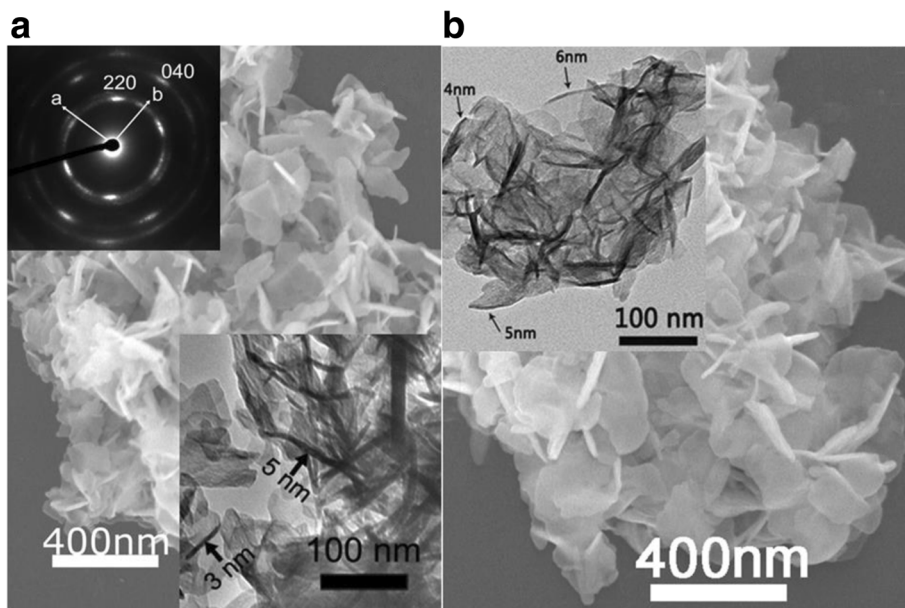


Fig. 2 SEM and TEM morphology of the products. SEM micrographs showing overall morphologies of the NO_3^- - $\text{L}(\text{Y}_{0.98}\text{Eu}_{0.02})\text{H}$ (a) and SO_4^{2-} - $\text{L}(\text{Y}_{0.98}\text{Eu}_{0.02})\text{H}$ (b) samples. The insets are the TEM morphology and selected area electron diffraction (SAED) pattern of the nanosheets

this work are nanometer thin, it shows a thermal behavior almost identical to that reported for thick crystals [25–29, 32–34]. The sulfate derivative similarly decomposes via three steps, but only up to the significantly higher temperature of $\sim 1135^\circ\text{C}$ and with a rather sluggish step in the ~ 175 – 1005°C range (stage II).

To better understand the thermal decomposition of SO_4^{2-} - $\text{L}(\text{Y}_{0.98}\text{Eu}_{0.02})\text{H}$, which has not been addressed prior to us, FTIR analysis was performed on the

products obtained at various selected temperatures for 4 h (Fig. 4). It is clearly seen that the powders calcined up to 900°C are characterized by strong SO_4^{2-} absorptions and successively weaker ones of hydroxyls/water. The results may thus imply that the sluggish weight loss observed on the TG curve from ~ 175 to 1005°C is mainly owing to successive dehydroxylation rather than desulfuration. The weight loss ($\sim 14.4\%$) calculated for dehydroxylation of $(\text{Y}_{0.98}\text{Eu}_{0.02})_2(\text{OH})_5(\text{SO}_4)_{0.5}$ to the nominal

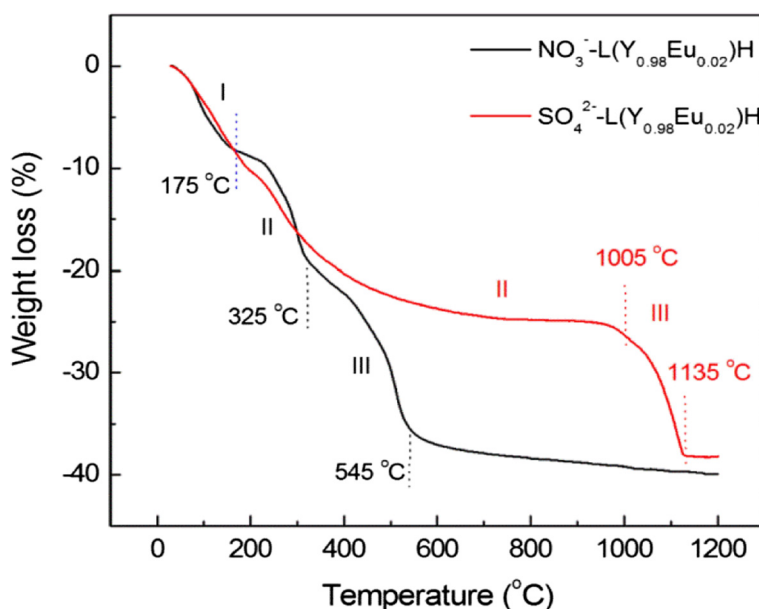


Fig. 3 TG curves of NO_3^- - and SO_4^{2-} -type $\text{L}(\text{Y}_{0.98}\text{Eu}_{0.02})\text{Hs}$. TG traces for the NO_3^- - and SO_4^{2-} -type $\text{L}(\text{Y}_{0.98}\text{Eu}_{0.02})\text{Hs}$

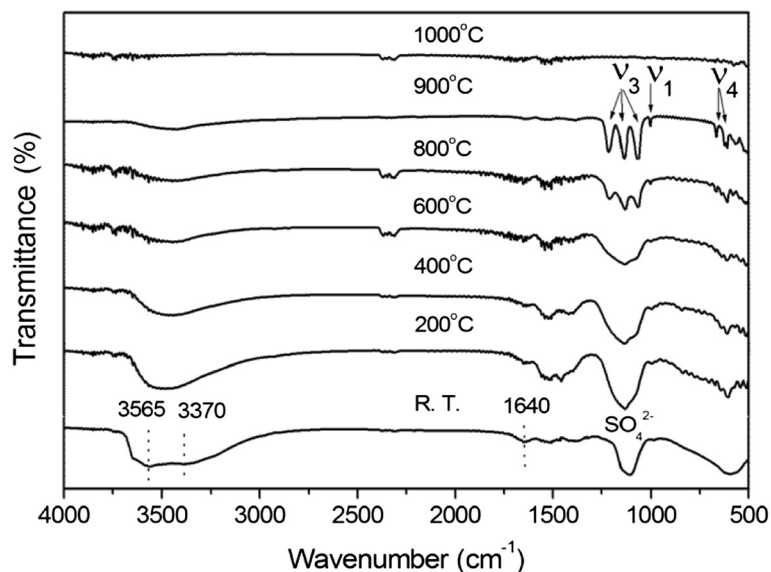


Fig. 4 FTIR spectra for the original $\text{SO}_4^{2-}\text{-L}(\text{Y}_{0.98}\text{Eu}_{0.02})\text{H}$ and the calcined products. FTIR spectra for the original $\text{SO}_4^{2-}\text{-L}(\text{Y}_{0.98}\text{Eu}_{0.02})\text{H}$ and the products calcined from it at various selected temperatures for 4 h

composition of $(\text{Y}_{0.98}\text{Eu}_{0.02})_2\text{O}_{2.5}(\text{SO}_4)_{0.5}$ is indeed close to that found via TG (~16.1 %). It is thus plausible to conclude that the slow dehydroxylation of $\text{SO}_4^{2-}\text{-L}(\text{Y}_{0.98}\text{Eu}_{0.02})\text{H}$ is mainly due to the intramolecular hydrogen bonding between SO_4^{2-} and OH^- groups. Raising the calcination temperature from 900 to 1000 °C simultaneously eliminates the strong SO_4^{2-} and the already rather weak hydroxyl absorptions, suggesting that the sudden weight loss observed on the TG curve from ~1005 to 1135 °C is dominantly resulted from desulfuration. Again, the weight

loss calculated for this thermal event (~14.9 %) is close to the value revealed by TG (~13.5 %). The SO_4^{2-} anions exhibit significantly split ν_3 and ν_4 vibrations for the 800 and 900 °C products, implying that the tetrahedrons of SO_4^{2-} are substantially distorted by direct coordination to Ln^{3+} [44, 45, 47–49].

Phase evolution of the $\text{SO}_4^{2-}\text{-L}(\text{Y}_{0.98}\text{Eu}_{0.02})\text{H}$ upon heating was studied via XRD analysis of the products calcined at different temperatures, and the results are displayed in Fig. 5. It is seen that dehydration of the

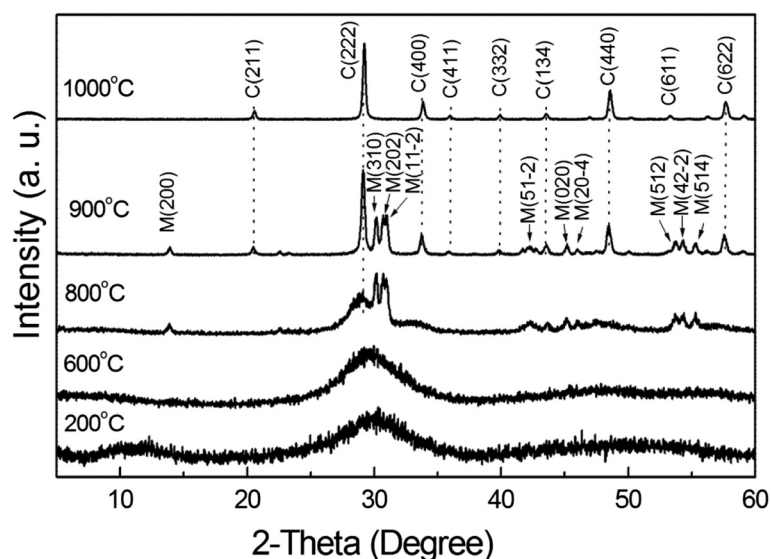


Fig. 5 XRD patterns of the products calcined from $\text{SO}_4^{2-}\text{-L}(\text{Y}_{0.98}\text{Eu}_{0.02})\text{H}$ at the different temperatures. XRD patterns of the products calcined from $\text{SO}_4^{2-}\text{-L}(\text{Y}_{0.98}\text{Eu}_{0.02})\text{H}$ at the different temperatures indicated in the figure, where letters C and M denote cubic $(\text{Y}_{0.98}\text{Eu}_{0.02})_2\text{O}_3$ and monoclinic $(\text{Y}_{0.98}\text{Eu}_{0.02})_2\text{O}_2\text{SO}_4$ phases, respectively

layered compound at 200 °C leads to an amorphous mass, which persists up to ~600 °C despite the already occurrence of dehydroxylation (Figs. 3 and 4). Further removal of hydroxyls at 800 °C produced a phase mixture of poorly crystallized cubic Ln_2O_3 ($\text{Ln} = \text{Y}_{0.98}\text{Eu}_{0.02}$, JCPDS: 00-043-1036) and monoclinic $\text{Ln}_2\text{O}_2\text{SO}_4$ (JCPDS: 00-053-0168), whose diffraction intensities both remarkably improve for the 900 °C product. As the original layered compound has the approximate composition of $\text{Ln}_2(\text{OH})_5(\text{SO}_4)_{0.5} \cdot n\text{H}_2\text{O}$, it can thus be said that the 900 °C product is approximately composed of 1/2 mol of $\text{Ln}_2\text{O}_2\text{SO}_4$ and 1/2 mol of Ln_2O_3 . Since the SO_4^{2-} in $\text{Ln}_2\text{O}_2\text{SO}_4$ is bidentately coordinated to Ln^{3+} [47–49], the significant splitting of the ν_3 and ν_4 IR bands was thus observed once the oxy-sulfate compound was formed (Fig. 4). The $\text{Ln}_2\text{O}_2\text{SO}_4$ component desulfurates at the higher temperature of 1000 °C, and thus, only cubic structured Ln_2O_3 was found. The results of XRD comply well with those of FTIR (Fig. 4). That is, the ν_3 and ν_4 vibrations of SO_4^{2-} present as single bands for the 200–600 °C products, as split bands for the 800 and 900 °C products, and vanish for the 1000 °C product. Similar phase evolution analysis of the $\text{NO}_3^- \text{-L}(\text{Y}_{0.98}\text{Eu}_{0.02})\text{H}$ found that cubic $(\text{Y}_{0.98}\text{Eu}_{0.02})_2\text{O}_3$ crystallizes at ~600 °C via an amorphous state at lower temperatures. The results are not shown here since they are essentially identical to those previously reported by us for thick $\text{NO}_3^- \text{-LRH}$ crystals [33].

Figure 6 compares XRD patterns of the oxides calcined from $\text{SO}_4^{2-} \text{-L}(\text{Y}_{0.98}\text{RE}_{0.02})\text{H}$ at 1100 °C for 4 h. Only enlarged view of the $2\theta = 25\text{--}35^\circ$ region was given to show the effects of RE^{3+} dopant. It is clearly seen that both

the (222) and (400) diffractions steadily shift to higher angles along with decreasing ionic radius of RE^{3+} , indicating the formation of solid solution. The lattice parameter (a , in angstrom) calculated from the strongest (222) diffraction indeed becomes successively smaller towards a smaller RE^{3+} (Fig. 6). The crystallite size assayed from the (222) diffraction by applying Scherrer equation is ~35 nm for all the oxides, irrespective of the dopant type. The cell parameters determined herein are all larger than the 10.547 Å reported for pure Y_2O_3 (JCPDS: 00-043-1036, Y^{3+} close to Ho^{3+} in radius), possibly owing to the limited crystallite size of the present powders.

Morphology evolution of the nanosheets during calcination was studied with $\text{NO}_3^- \text{-L}(\text{Y}_{0.98}\text{Eu}_{0.02})\text{H}$ and $\text{SO}_4^{2-} \text{-L}(\text{Y}_{0.98}\text{Eu}_{0.02})\text{H}$ for example. Figure 7 exhibits typical FE-SEM morphologies for the powders calcined at some representative temperatures. It is seen that the 800 °C product from $\text{NO}_3^- \text{-L}(\text{Y}_{0.98}\text{Eu}_{0.02})\text{H}$ well retained the overall morphology of its precursor, despite that it has been a phase-pure oxide, and the flower-like assemblies (domains) and the individual nanosheets within the domains are clearly observable. Calcination at 900 °C led to substantial collapse of the nanosheets into nanoparticles within each domain, owing to the thermal stress arising from crystallite growth, and the domain boundary is still identifiable. Significant crystallite growth was observed at 1100 °C, together with densification of some of the domains via inter-particle sintering to form dense aggregates. The final powder was found to have a specific surface area of ~8.3 m²/g, corresponding to an average

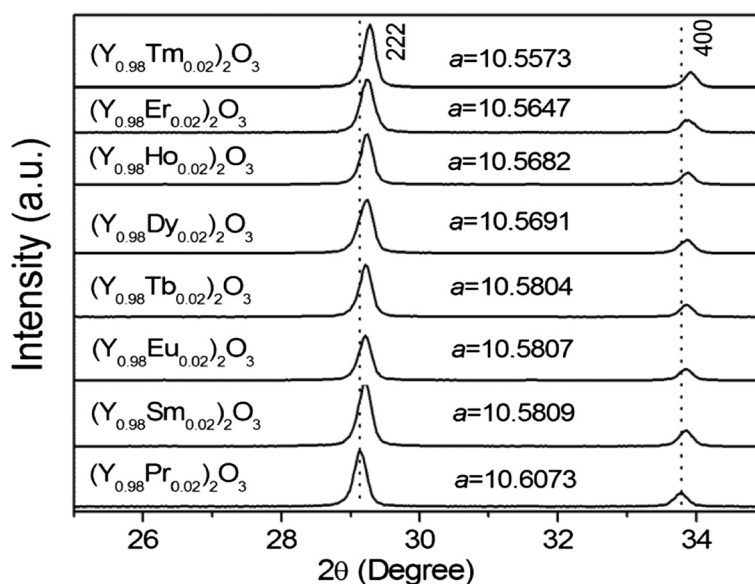


Fig. 6 XRD patterns of the $(\text{Y}_{0.98}\text{RE}_{0.02})_2\text{O}_3$ powders. XRD patterns of the $(\text{Y}_{0.98}\text{RE}_{0.02})_2\text{O}_3$ powders calcined from $\text{SO}_4^{2-} \text{-L}(\text{Y}_{0.98}\text{RE}_{0.02})\text{H}$ at 1100 °C for 4 h, with the cell parameter a (in angstrom) included

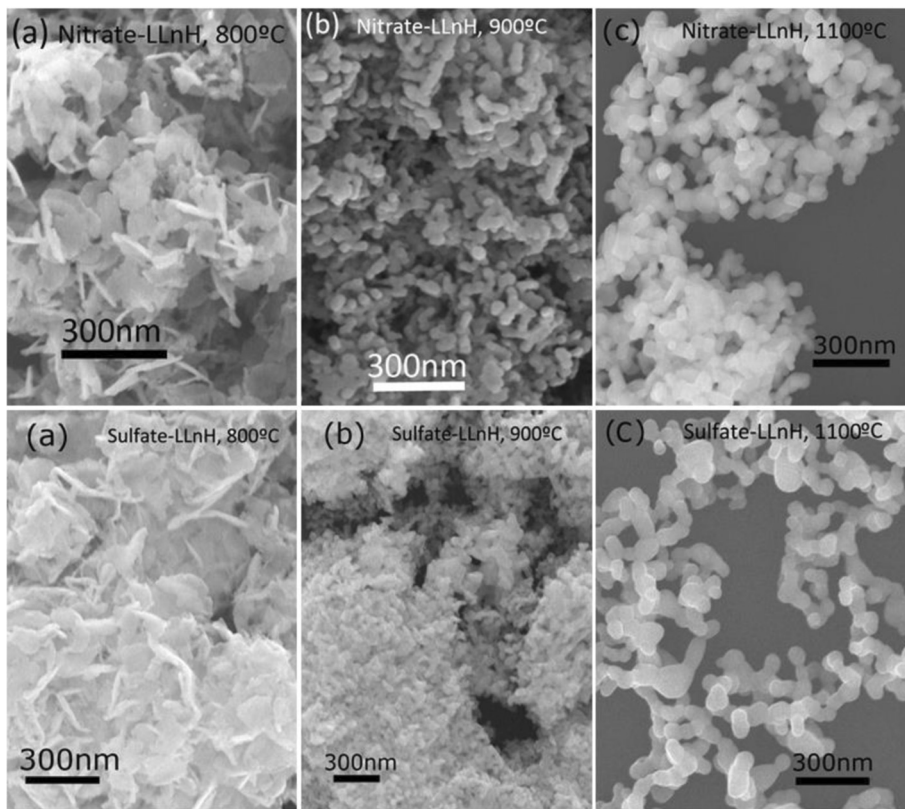


Fig. 7 FE-SEM micrographs of the products calcined from NO_3^- - and SO_4^{2-} - $\text{L}(\text{Y}_{0.98}\text{Eu}_{0.02})\text{Hs}$ at the temperatures for (a) 800 °C, (b) 900 °C and (c) 1100 °C

particle size of ~ 140 nm. The value is significantly larger than that observed from the FE-SEM micrograph (up to ~ 90 nm) for the primary particles, due to the presence of hard aggregates. The 800 and 900 °C powders from SO_4^{2-} - $\text{L}(\text{Y}_{0.98}\text{Eu}_{0.02})\text{H}$ show

morphologies similar to their counterparts described above, except that the domains in the 900 °C product are much less disintegrated since the $\text{Ln}_2\text{O}_2\text{SO}_4$ phase (Fig. 5), finely mixed with the Ln_2O_3 portion, significantly restricts crystallite growth. Calcination

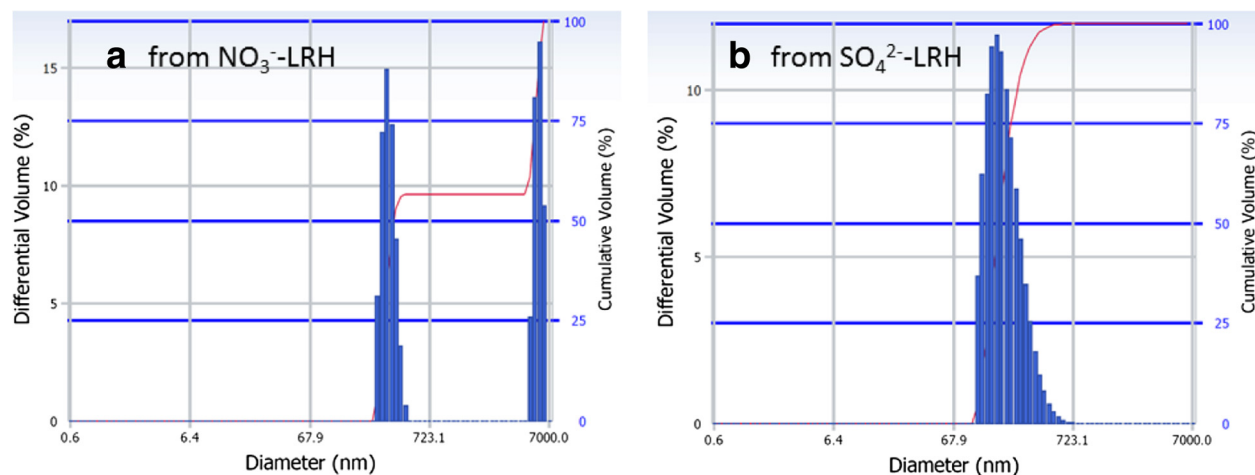
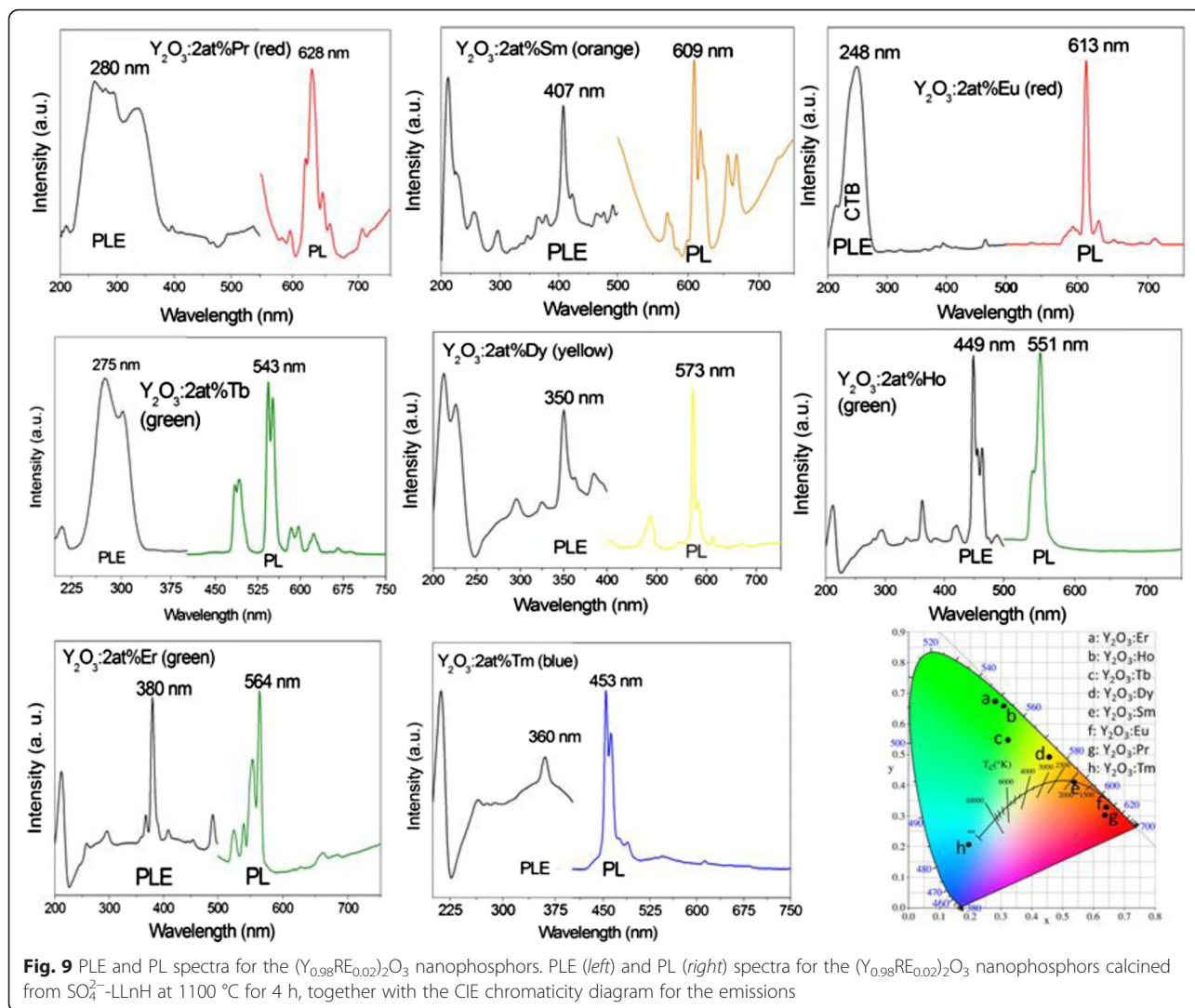


Fig. 8 Particle size/size distribution analysis of the $(\text{Y}_{0.98}\text{Eu}_{0.02})_2\text{O}_3$ powders. Particle size/size distribution analysis of the $(\text{Y}_{0.98}\text{Eu}_{0.02})_2\text{O}_3$ powders calcined at 1100 °C for 4 h from **a** the NO_3^- - $\text{L}(\text{Y}_{0.98}\text{Eu}_{0.02})\text{H}$ and **b** the SO_4^{2-} - $\text{L}(\text{Y}_{0.98}\text{Eu}_{0.02})\text{H}$. The size distribution is given in cumulative volume (right axis)



to 1100 °C causes complete collapse of the domains to yield a substantially better dispersed oxide powder, and the evolution of SO_x gas was believed to promote disintegration of the domains. Accordingly, the final oxide has a much higher specific surface area of $\sim 17.5 \text{ m}^2/\text{g}$ (average particle size $\sim 67 \text{ nm}$).

The amount of residual sulfur in the oxide phosphors calcined at 1100 °C was assayed via ICP elemental analysis to be up to 0.18 wt.% in our previous work [50].

Figure 8 shows the particle size/size distribution of the two kinds of $(Y_{0.98}Eu_{0.02})_2O_3$ powders calcined at 1100 °C.

Table 1 Optical properties of the $(Y_{0.98}RE_{0.02})_2O_3$ nanophosphors

RE	Main PLE band (nm)	Main PL band (nm)	CIE coordinates (x,y)	Emission color	Lifetime
Pr	280, $4f^2 \rightarrow 4f^15d^1$	645, $^1D_2 \rightarrow ^3H_4$	(0.639,0.303)	Deep red	160 ± 13 ns
Sm	407, $^6H_{5/2} \rightarrow ^4K_{11/2}$	609, $^4G_{5/2} \rightarrow ^6H_{7/2}$	(0.538,0.414)	Orange	1.52 ± 0.01 ms
Eu	250, CTB ($O^{2-} \rightarrow Eu^{3+}$)	613, $^5D_0 \rightarrow ^7F_2$	(0.640,0.329)	Orange red	2.71 ± 0.02 ms
Tb	275, $4f^8 \rightarrow 4f^75d^1$	545, $^5D_4 \rightarrow ^7F_5$	(0.321,0.551)	Green	3.08 ± 0.02 ms
Dy	350, $^6H_{15/2} \rightarrow ^6P_{7/2}$	573, $^4F_{9/2} \rightarrow ^6H_{13/2}$	(0.457,0.492)	Yellow	229 ± 12 ns
Ho	449, $^5I_8 \rightarrow ^5F_1$	551, $^5S_2 \rightarrow ^5I_8$	(0.308,0.657)	Green	126 ± 9 ns
Er	380, $I_{15/2} \rightarrow ^4G_{11/2}$	564, $^4S_{3/2} \rightarrow ^4I_{15/2}$	(0.281,0.675)	Green	246 ± 15 ns
Tm	360, $^3H_6 \rightarrow ^1D_2$	453, $^1D_2 \rightarrow ^3F_4$	(0.194,0.206)	Blue	170 ± 13 ns

A summary of optical properties of the $(Y_{0.98}RE_{0.02})_2O_3$ nanophosphors

It is clearly seen that the powder from $\text{NO}_3^- \text{-L}(\text{Y}_{0.98}\text{Eu}_{0.02})\text{H}$ exhibits a bimodal size distribution owing to the presence of hard aggregates (Fig. 7). The finer portion (~ 56.5 vol.%) has an average particle (cluster) size of $\sim 320 \pm 43$ nm while the coarser part has a value of $\sim 6.21 \pm 0.53$ μm . A unimodal size distribution was observed for the $(\text{Y}_{0.98}\text{Eu}_{0.02})_2\text{O}_3$ powder from $\text{SO}_4^{2-} \text{-L}(\text{Y}_{0.98}\text{Eu}_{0.02})\text{H}$, and the average particle size was analyzed to be $\sim 219 \pm 94$ nm. The above results are in agreement with morphology observations (Fig. 7), and further confirm that SO_4^{2-} exchange of the interlayer NO_3^- is beneficial to the derivation of finer and better dispersed oxide powders.

Photoluminescent Properties of the $(\text{Y}_{0.98}\text{RE}_{0.02})_2\text{O}_3$ Nanophosphors

Figure 9 shows photoluminescence excitation/emission spectra for the $(\text{Y}_{0.98}\text{RE}_{0.02})_2\text{O}_3$ nanophosphors calcined at 1100 °C, with the excitation and emission wavelengths used for the measurements indicated in each part of the figure. The origins of these main bands [19, 51–53] are summarized in Table 1, together with the chromaticity coordinates of emission and the fluorescence lifetime. The origins of the other PLE/PL bands in each part of Fig. 9 are well documented and can be found in the literature [19, 51–53]. It is seen from the Commission Internationale de l'Éclairage (CIE) chromaticity diagram that the phosphors synthesized in this work span a wide range of emission colors, from blue (Tm^{3+}) to deep red (Pr^{3+}) via green (Tb^{3+} , Ho^{3+} , and Er^{3+}), yellow (Dy^{3+}), orange (Sm^{3+}), and orange red (Eu^{3+}).

Conclusions

It is shown in this work that coprecipitation at the freezing temperature of ~ 4 °C can directly produce, without exfoliation, solid-solution nanosheets of the nitrate-type layered hydroxides of $\text{Ln}_2(\text{OH})_5\text{NO}_3 \cdot n\text{H}_2\text{O}$ ($\text{NO}_3^- \text{-LLnH}$, $\text{Ln} = \text{Y}_{0.98}\text{RE}_{0.02}$, and $\text{RE} = \text{Pr}$, Sm , Eu , Tb , Dy , Ho , Er , and Tm). Replacement of the interlayer NO_3^- with SO_4^{2-} via in situ anion exchange was achieved to produce the sulfate derivative of $\text{SO}_4^{2-} \text{-LLnH}$. Detailed characterizations of both the types of layered materials and their calcination products via the combined techniques of XRD, FTIR, DTA/TG, FE-SEM/TEM, BET, particle sizing, and photoluminescence spectroscopy have led to the following main conclusions: (1) anion exchange did not bring about any appreciable change to the layered structure and the two-dimensional crystallite morphology, but induces a basal-spacing contraction from ~ 0.886 to 0.841 nm, (2) the interlayer SO_4^{2-} significantly raises the decomposition temperature of the nanosheets from ~ 600 to 1000 °C to yield oxide via a monoclinic-structured $\text{Ln}_2\text{O}_2\text{SO}_4$ intermediate phase, and (3) the $(\text{Y}_{0.98}\text{RE}_{0.02})_2\text{O}_3$ powders from $\text{SO}_4^{2-} \text{-LLnH}$ are much better dispersed and finer than those from $\text{NO}_3^- \text{-LLnH}$, and exhibit emission

colors, depending on RE^{3+} , covering a wide range in the CIE chromaticity diagram, from blue to deep red via green, yellow, orange, and orange red.

Acknowledgements

The work is supported in part by the National Natural Science Foundation of China (Grants No. 51172038, 51302032, and 51402059), the Fundamental Research Funds for the Central Universities (Grants N140204002 and N130810003) and Grants-in-Aid for Scientific Research (KAKENHI, No.26420686).

Authors' contributions

JGL conceived the project and drafted the manuscript. XLW and WGL carried out the experiments. QZ, XDL and XDS were involved in sample characterization and results discussion. All the authors have read and approved the final manuscript.

Competing interests

The authors declare that they have no competing interests.

Author details

¹Key Laboratory for Anisotropy and Texture of Materials (Ministry of Education), School of Materials Science and Engineering, Northeastern University, Shenyang, Liaoning 110819, China. ²Materials Processing Unit, National Institute for Materials Science, Tsukuba, Ibaraki 305-0044, Japan. ³College of Material Science and Engineering, Guilin University of Technology, Guilin, Guangxi 541004, China.

Received: 20 May 2016 Accepted: 5 July 2016

Published online: 12 July 2016

References

- Igarashi T, Ihara M, Kusunoki T, Ohno K (2000) Relationship between optical properties and crystallinity of nanometer $\text{Y}_2\text{O}_3:\text{Eu}^{3+}$ phosphor. *Appl Phys Lett* 76:1549–1551
- Zhu Q, Li JG, Li XD, Sun XD (2009) Morphology-dependent crystallization and luminescence behavior of (Y, Eu) $_2\text{O}_3$ red phosphors. *Acta Mater* 57:5975–5985
- Blasse G, Grabmair BC (1994) *Luminescent materials*. Springer Verlag, Berlin
- Hong GY, Jeon BS, Yoo YK, Yoo JS (2001) Photoluminescence characteristics of spherical $\text{Y}_2\text{O}_3:\text{Eu}^{3+}$ phosphors by aerosol pyrolysis. *J Electrochem Soc* 148:H161–H166
- Ekambaram S, Patil KC, Mazza M (2005) Synthesis of lamp phosphors: facile combustion approach. *J Alloys Compd* 393:81–92
- Kim EJ, Kang YC, Park HD, Ryu SK (2003) UV and VUV characteristics of (Y,Gd) $_2\text{O}_3:\text{Eu}$ phosphor particles prepared by spray pyrolysis from polymeric precursors. *Mater Res Bull* 38:515–524
- Lenggoro IW, Itoh Y, Okuyama K, Kim TO (2004) Nanoparticles of a doped oxide phosphor prepared by direct-spray pyrolysis. *J Mater Res* 19:3534–3539
- Wakefield G, Holland E, Dobson PJ, Hutchison JL (2001) Luminescence properties of nanocrystalline $\text{Y}_2\text{O}_3:\text{Eu}^{3+}$. *Adv Mater* 13:1557–1560
- Camenzind A, Strobel R, Pratsinis SE (2005) Cubic or monoclinic $\text{Y}_2\text{O}_3:\text{Eu}^{3+}$ nanoparticles by one step flame spray pyrolysis. *Chem Phys Lett* 415:193–197
- Li J-G, Ishigaki T (2012) One-step Ar/O_2 thermal plasma processing of $\text{Y}_2\text{O}_3:\text{Eu}^{3+}$ red phosphors: phase structure, photoluminescent properties, and the effects of Sc^{3+} codoping. *J Solid State Chem* 196:58–62
- Li J-G, Li XD, Sun XD, Ishigaki T (2008) Monodispersed colloidal spheres for uniform $\text{Y}_2\text{O}_3:\text{Eu}^{3+}$ red-phosphor particles and greatly enhanced luminescence by simultaneous Gd^{3+} doping. *J Phys Chem C* 112:11707–11716
- Zhu Q, Li J-G, Li XD, Sun XD, Sakka Y (2011) Monodisperse colloidal spheres for (Y, Eu) $_2\text{O}_3$ red-emitting phosphors: establishment of processing window and size-dependent luminescence behavior. *Sci Technol Adv Mater* 12:055001
- Wu CF, Qin WP, Qin GS (2003) Photoluminescence from surfactant-assembled $\text{Y}_2\text{O}_3:\text{Eu}^{3+}$ nanotubes. *Appl Phys Lett* 82:520–522
- Zhang JL, Hong GY (2004) Synthesis and photoluminescence of the $\text{Y}_2\text{O}_3:\text{Eu}^{3+}$ phosphor nanowires in AAO template. *J Solid State Chem* 177:1292–1296
- Wan JX, Wang ZH, Chen XY, Mu LY, Qian YT (2005) Shape-tailored photoluminescent intensity of red phosphor $\text{Y}_2\text{O}_3:\text{Eu}^{3+}$. *J Cryst Growth* 284:538–543
- He Y, Tian Y, Zhu ZF (2003) Large-scale synthesis of luminescent $\text{Y}_2\text{O}_3:\text{Eu}$ nanobelts. *Chem Lett* 32:862–863

17. Wu X, Tao Y, Gao F, Dong L, Hu Z (2005) Preparation and photoluminescence of yttrium hydroxide and yttrium oxide doped with europium nanowires. *J Cryst Growth* 277:643–649
18. Lu ZG, Qian DY, Tang G (2005) Facile synthesis and characterization of sheet-like $Y_2O_3:Eu^{3+}$ microcrystals. *J Cryst Growth* 276:513–518
19. Lin J, Yu M, Lin CK, Liu XM (2007) Multifunctional oxide optical materials via the versatile Pechini-type sol-gel process: synthesis and characteristics. *J Phys Chem C* 111:5835–5845
20. Gándara F, Perles J, Snecko N, Iglesias M, Gómez-Lor B, Gutiérrez-Puebla E et al (2006) Layered rare-earth hydroxides: a class of pillary crystalline compounds for intercalation chemistry. *Angew Chem Int Ed* 45:7998–8001
21. Geng FX, Matsushita Y, Ma R, Xin H, Tanaka M, Izumi F, Iyi N, Sasaki T (2008) General synthesis and structural evolution of a layered family of $Ln_8(OH)_{20}C_{14}nH_2O$ ($Ln = Nd, Sm, Eu, Gd, Tb, Dy, Ho, Er, Tm, and Y$). *J Am Chem Soc* 130:16344–16350
22. Geng FX, Xin H, Matsushita Y et al (2008) New layered rare-earth hydroxides with anion-exchange properties. *Chem Eur J* 14:9255–9260
23. Geng FX, Matsushita Y, Ma R et al (2008) General synthesis and structural evolution of a layered family of $Ln_8(OH)_{20}C_{14}nH_2O$ ($Ln = Nd, Sm, Eu, Gd, Tb, Dy, Ho, Er, Tm, and Y$). *Inorg Chem* 130:16344–16350
24. Geng FX, Ma R, Sasaki T (2010) Anion-exchangeable layered materials based on rare-earth phosphors: unique combination of rare-earth host and exchangeable anions. *Acc Chem Res* 43:1177–1185
25. McIntyre LJ, Jackson LK, Fogg AM (2008) Synthesis and anion exchange chemistry of new intercalation hosts containing lanthanide cations, $Ln_2(OH)_2NO_3 \cdot nH_2O$ ($Ln = Y, Gd-Lu$). *J Phys Chem Solids* 69:1070–1074
26. Poudret L, Prior TJ, McIntyre LJ et al (2008) Synthesis and crystal structures of new lanthanide hydroxylate anion exchange materials, $Ln_2(OH)_2X \cdot 1.5H_2O$ ($X = Cl, Br; Ln = Y, Dy, Er, Yb$). *Chem Mater* 20:7447–7453
27. McIntyre LJ, Jackson LK, Fogg AM (2008) $Ln_2(OH)_2NO_3 \cdot xH_2O$ ($Ln = Y, Gd-Lu$): a novel family of anion exchange intercalation hosts. *Chem Mater* 20:335–340
28. Hindocha SA, McIntyre LJ, Fogg AM (2009) Precipitation synthesis of lanthanide hydroxyl nitrate anion exchange materials, $Ln_2(OH)_2NO_3 \cdot H_2O$ ($Ln = Y, Eu-Er$). *J Solid State Chem* 182:1070–1074
29. McIntyre LJ, Prior TJ, Fogg AM (2010) Observation and isolation of layered and framework ytterbium hydroxide phases using in situ energy-dispersive X-ray diffraction. *Chem Mater* 22:2635–2645
30. Lee K-H, Byeon S-H (2009) Extended member of the layered rare-earth hydroxides family, $RE_2(OH)_2NO_3 \cdot nH_2O$ ($RE = Sm, Eu, and Gd$): synthesis and anion-exchange behavior. *Eur J Inorg Chem* 7:929–936
31. Lee K-H, Byeon S-H (2009) Synthesis and aqueous colloidal solutions of $RE_2(OH)_2NO_3 \cdot nH_2O$ ($RE = Nd$ and La). *Eur J Inorg Chem* 31:4727–4732
32. Zhu Q, Li J-G, Zhi CY, Ma RZ, Sasaki T, Xu JX, Liu CH, Li XD, Sun XD, Sakka Y (2011) Nanometer-thin layered hydroxide platelets of $(Y_{0.95}Eu_{0.05})_2(OH)_2NO_3 \cdot xH_2O$: exfoliation-free synthesis, self-assembly, and the derivation of dense oriented oxide films of high transparency and greatly enhanced luminescence. *J Mater Chem* 21:6903–6908
33. Zhu Q, Li J-G, Zhi CY, Li XD, Sun XD, Sakka Y, Golberg D, Bando Y (2010) Layered rare-earth hydroxides (LRHs) of $(Y_{1-x}Eu_x)_2(OH)_2NO_3 \cdot nH_2O$ ($x = 0-1$): structural variations by Eu^{3+} doping, phase conversion to oxides, and the correlation of photoluminescence behaviors. *Chem Mater* 22:4204–4213
34. Zhu Q, Li J-G, Ma RZ, Sasaki T, Yang XJ, Li XD, Sun XD, Sakka Y (2012) Well-defined crystallites autoclaved from the nitrate/ NH_4OH reaction system as the precursor for $(Y, Eu)_2O_3$ red phosphor: crystallization mechanism, phase and morphology control, and luminescent property. *J Solid State Chem* 192:229–237
35. Hu LF, Ma RZ, Ozawa TC, Sasaki T (2010) Exfoliation of layered europium hydroxide into unilamellar nanosheets. *Chem Asian J* 5:248–251
36. Lee KH, Lee BI, You JH, Byeon SH (2010) Transparent $Gd_2O_3:Eu$ phosphor layer derived exfoliated layered gadolinium hydroxide nanosheets. *Chem Commun* 46:1461–1463
37. Yoon YS, Byeon SH, Lee IS (2010) Unexplored thermal transformation behavior of two-dimensionally bound gadolinium hydroxide layers: fabrication of oriented crystalline films of gadolinium oxychloride nanosheets suitable for the multicolor luminescence with color tenability. *Adv Mater* 22:3272–3276
38. Lee BI, Lee ES, Byeon SH (2012) Assembly of layered rare-earth hydroxide nanosheets and SiO_2 nanoparticles to fabricate multifunctional transparent films capable of combinatorial color generation. *Adv Funct Mater* 22:3562–3569
39. Zhu Q, Li JG, Li XD, Sun XD, Qi Y, Zhu MY et al (2014) Tens of micron sized unilamellar nanosheets of Y/Eu layered rare-earth hydroxide (LRH): efficient exfoliation via fast anion exchange and their self-assembly into oriented oxide film with enhanced photoluminescence. *Sci Technol Adv Mater* 15:014203
40. Wu XL, Li J-G, Zhu Q, Li JK, Ma R, Sasaki T, Li XD, Sun XD, Sakka Y (2012) The effects of Gd^{3+} substitution on the crystal structure, site symmetry, and photoluminescence of Y/Eu layered rare-earth hydroxide (LRH) nanoplates. *Dalton Trans* 41:1854–1861
41. Wu XL, Li J-G, Li JK, Zhu Q, Li XD, Sun XD et al (2013) Layered rare-earth hydroxide (LRH) and oxide nanoplates of the Y/Tb/Eu system: phase controlled processing, structure characterization, and color-tunable photoluminescence via selective excitation and efficient energy transfer. *Sci Technol Adv Mater* 14:015006
42. Wu XL, Li J-G, Ping D-H, Li JK, Zhu Q, Li XD, Sun XD, Sakka Y (2013) Structure characterization and photoluminescence properties of $(Y_{0.95-x}Gd_xEu_{0.05})_2O_3$ red phosphors converted from layered rare-earth hydroxide (LRH) nanoflake precursors. *J Alloys Compd* 559:188–195
43. Wu XL, Li J-G, Zhu Q, Liu WG, Li J, Li XD, Sun XD, Sakka Y (2015) One-step freezing temperature crystallization of layered rare-earth hydroxide $(Ln_2(OH)_2NO_3 \cdot nH_2O)$ nanosheets for a wide spectrum of Ln ($Ln = Pr-Er, and Y$), anion exchange with fluorine and sulfate, and microscopic coordination probed via photoluminescence. *J Mater Chem C* 3:3428–3437
44. Nakamoto K (1963) *Infrared spectra of inorganic and coordination compounds*. John Wiley & Sons, New York
45. Gadsden JA (1975) *Infrared spectra of minerals and related inorganic compounds*. Butterworth, Newton
46. Shannon RD (1976) Revised effective ionic radii and systematic studies of interatomic distances in halides and chalcogenides. *Acta Crystallogr Sect A Cryst Phys Diffr Theor Gen Crystallogr* A32:751–767
47. Liang JB, Ma R, Geng FX, Ebina Y, Sasaki T (2010) $Ln_2(OH)_2SO_4 \cdot nH_2O$ ($Ln = Pr$ to $Tb; n \sim 2$): a new family of layered rare-earth hydroxides rigidly pillared by sulfate ions. *Chem Mater* 22:6001–6007
48. Wang XJ, Li J-G, Zhu Q, Li XD, Sun XD, Sakka Y (2014) Facile and green synthesis of $(La_{0.95}Eu_{0.05})_2O_3S$ red phosphors with sulfate-ion pillared layered hydroxides as a new type of precursor: controlled hydrothermal processing, phase evolution and photoluminescence. *Sci Technol Adv Mater* 15:014204
49. Wang XJ, Li J-G, Zhu Q, Li XD, Sun XD, Sakka Y (2014) Synthesis, characterization, and photoluminescent properties of $(La_{0.95}Eu_{0.05})_2O_3SO_4$ red phosphors with layered hydroxyl sulfate as precursor. *J Alloys Compd* 603:28–34
50. Lu B, Li J-G, Suzuki TS, Estili M, Liu WG, Sun XD, Sakka Y (2015) Controlled synthesis of layered rare-earth hydroxide nanosheets leading to highly transparent $(Y_{0.95}Eu_{0.05})_2O_3$ ceramics. *J Am Ceram Soc* 98(5):1413–1422
51. Li J-G, Sakka Y (2015) Recent progress in advanced optical materials based on gadolinium aluminate garnet $(Gd_3Al_2O_{12})$. *Sci Technol Adv Mater* 16:014902
52. Yang J, Li C, Quan Z, Zhang C, Yang P, Li Y, Yu C, Lin J (2008) Self-assembled 3D flowerlike Lu_2O_3 and $Lu_2O_3:Ln^{3+}$ ($Ln = Eu, Tb, Dy, Pr, Sm, Er, Ho, Tm$) microarchitectures: ethylene glycol-mediated hydrothermal synthesis and luminescent properties. *J Phys Chem C* 112:12777–12785
53. Aumuller GC, Kostler W, Grabmaier BC, Grey R (1994) Luminescence properties of Pr^{3+} in cubic rare-earth-oxides. *J Phys Chem Solids* 55:767–772

Submit your manuscript to a SpringerOpen® journal and benefit from:

- Convenient online submission
- Rigorous peer review
- Immediate publication on acceptance
- Open access: articles freely available online
- High visibility within the field
- Retaining the copyright to your article

Submit your next manuscript at ► springeropen.com